

Novel Percolation-based Measure for Fibre Efficacy in FRC Beams

Asghar Aryanfar^{*†‡}, Irem Sanal[†], Jaime Marian[‡]

[†] *California Institute of Technology, 1200 E California Blvd, Pasadena, CA 91125*

[‡] *Bahçeşehir University, 4 Çırağan Cad, Beşiktaş, Istanbul, Turkey 34349*

[‡] *University of California, 410 Westwood Plaza, Los Angeles, CA 90095*

Abstract

The Fibre-reinforced concrete exhibits a heterogeneous microstructure that forms an aggregate/fibre/matrix composite, where the flexural stress from the external forces typically leads to cracking and fracture. We develop a computational measure for predicting the fibre's efficacy by means of the energy absorbed within the initiated area of the cracks. We verify the analytical development for the experimental data by means of the literature and we justify the results with numerical simulations in the elastic regime. Our development couples the localization of the stress in the crack tip with the random distribution cracks which leads to the spatial strain field. Such percolation based quantification of the cracks on the the early-stage particularly is useful for effective utilization of fibres during extended propagation.

Keywords: Fibre reinforcement, Percolation, Fracture, Absorbed energy.

*Corresponding author; email: aryanfar@caltech.edu

Parameter	L	W	H	a	σ_y	L_f	D_f	Δt
Value	400	100	{25,40,65,100}	50	2000	{6,13}	0.16	15
Unit	mm	mm	mm	mm	MPa	mm	mm	s

Table 1: Experimental parameters.

1 Introduction

Fibre-reinforced concrete (FRC) is one of the most popular innovations in the concrete technology. The addition of short, discrete fibres provides enhanced properties to this composite cement-based material [1, 2]. The inclusion of steel fibres significantly improves the tensile behavior of microcracks by reducing their widths and spacing [3, 4, 5]. The bridging stretched fibres increase the post-cracking residual strength of concrete and counter-act the crack propagation. Moreover, due to the de-bonding and pull-out mechanisms of the fibres, a greater amount of energy is dissipated, strengthening the toughness significantly. This enhanced behavior is mainly influenced by the amount of bridging fibres and their mechanical properties, even at low dosages. [6, 7, 8]

Recent studies have determined the role of fibre orientation and distribution on the holding stress for enhancing the post-cracking flexural strength. [9, 10] The the image processing techniques have monitored the role of fibres as a non-destructive method [11, 12] and the crack patterns have been estimated from external surfaces. [13]

The fracture in FRC initially starts by the formation of microcracks, mainly due to inhomogeneity, anisotropy and stress localization. This process consumes large amount of energy and slows down the propagation rate. The crack region can be divided to *frontal zone* which is localized ahead of the main crack that forms the microcracks with possibility of large branching, depending on the micro-structure, [14] whereas the following *wake region* includes the fracture surface and is controlled either by bridging of fibres or their pull-out friction.[15, 16] At the Fibre-bridging zone, only the fibres carry all post-cracking loads taken by the composite.[17, 18] Yet, more information and versatile method on the quantitative capacity of fibres would highly benefit the controlling crack initiation and propagation.

In this paper, we introduce a new measure for the efficacy of the fibres in FRC using the initial area of the formed cracks. Such randomly-propagated medium has been captured

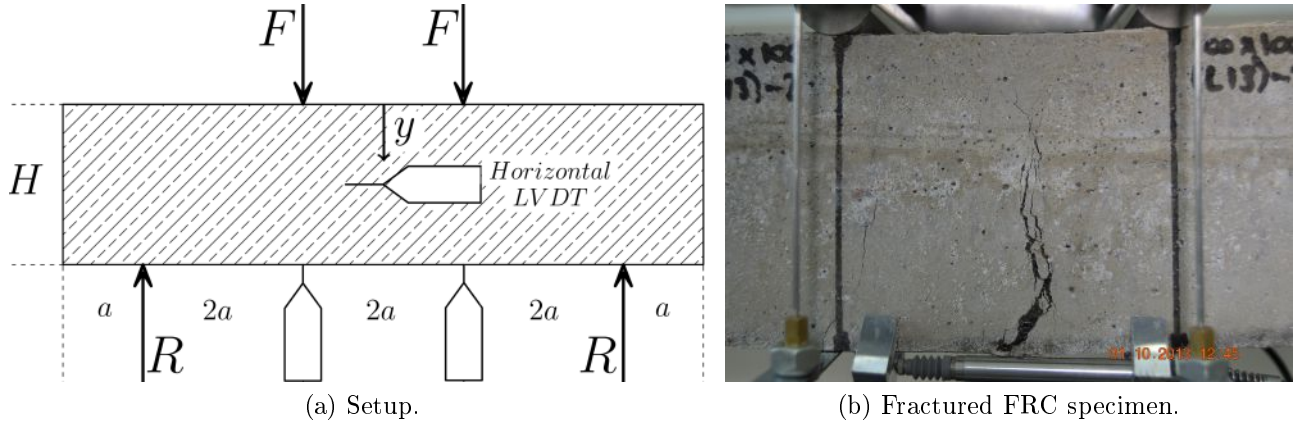


Figure 1: Experimental procedure.

using our percolation paradigm. The bridging between the geometry of the fracture and the mechanics (i.e. loading) is provided by distinguishing the applied and absorbed energies during the original inception of cracks. The method has been implemented to our experimental data on four-point flexural loading. We have quantified the ability of the fibres to bridge the cracks in the span of the crack development and our results have been verified with the analogous recent studies in the literature.

2 Methodology

2.1 Experimental / Numerical computations

In order to obtain the crack effectiveness of the fibres, experimental concrete mixes were cast with water-binder ratio of $w/b = 0.24$ and 1.7% added dosage of super-plasticizer. The desired cement-based mixture was fabricated in the mortar mixtures with the following proportions:¹

$$\text{Cement} : \text{Sand} : \text{Slag} : \text{Water} : \text{Plasticizer} : \text{Fiber} \equiv 98 : 1114 : 418 : 220 : 18 : 94.8$$

where the cement type is *CEM*|42.5*R* and the super-plasticizer is polycarboxylate-based. The FRC concretes were produced and cured (28 days, $RH > 90\%$, $T = 20 \pm 2^\circ C$). The length L , width W and height H of the specimen is given in Table 1 as well as the fibre length

¹Densities of the materials are 3.14, 2.65, 2.92, 10.075 and 7.17kg/m³ respectively.

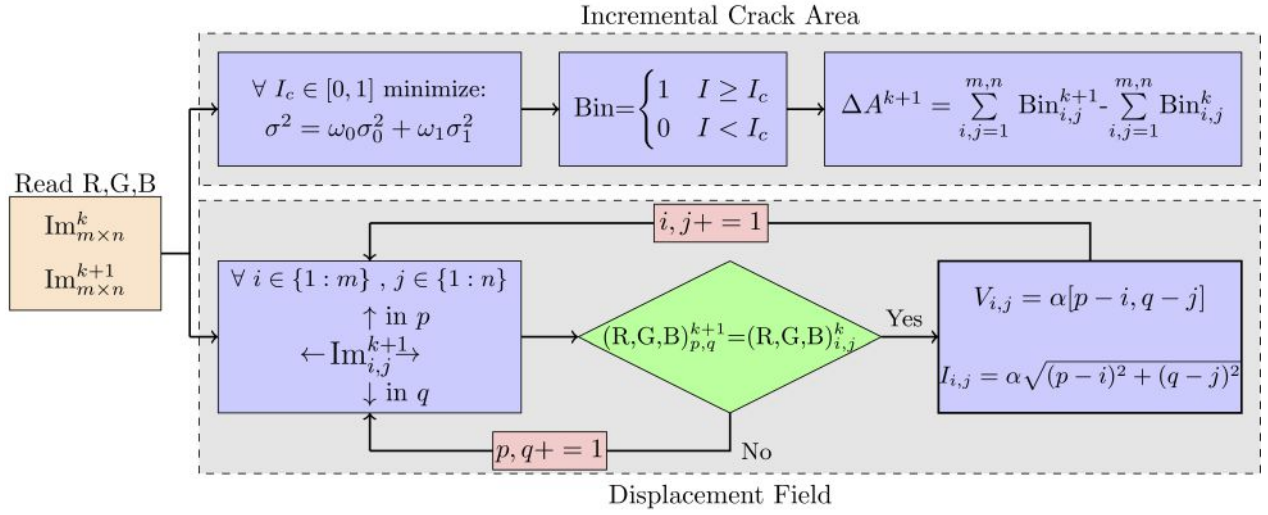


Figure 2: Pseudo-code for image processing. (ΔA : incremental area. V : displacement vector. I : displacement value.)

59 L_f diameters D_f ², the tensile stress σ_y . The distance parameter a and the measurement
60 time interval Δt are included as well.

61 The beam specimens were tested in four-point bending, according to Figure 1a, using an
62 MTS Closed-Loop Displacement Controlled Servo Hydraulic Testing Machine with capacity
63 of 100kN. Four Linear Variable Displacement Transducers (LVDTs) were mounted verti-
64 cally under the specimen to measure the average deflection and two LVDTs were mounted
65 horizontally just on the opposite sides of loading region of the specimen to measure average
66 crack mouth opening displacement. These LVDTs also provided feedback to the servo-valve
67 for closed-loop control in the test. For crack monitoring, a camera was placed perpendicular
68 to the beam face at 28cm the illumination was carried out using a white light projector. Suc-
69 cessive digital images were taken from each beam specimen undergoing deformation during
70 using linear scan high resolution charged coupled (CCD) camera in successive intervals of
71 . $\Delta t = 15s$. The images were compared with the original undeformed reference image to
72 obtain the variation in the crack area and the local displacements. Loading was applied at
73 LVDT-controlled displacement rate of 0.01mm/min, until the opening of the crack reached
74 half the fibre length. ($w_{max} \sim L_f$). Such experimental data were used to identify the *effective*
75 *cracks* as well as the *displacement field* within the sample in the span of time, as shown in
76 Figure 2.

²Aspect ratio := {81.25, 37.5}.

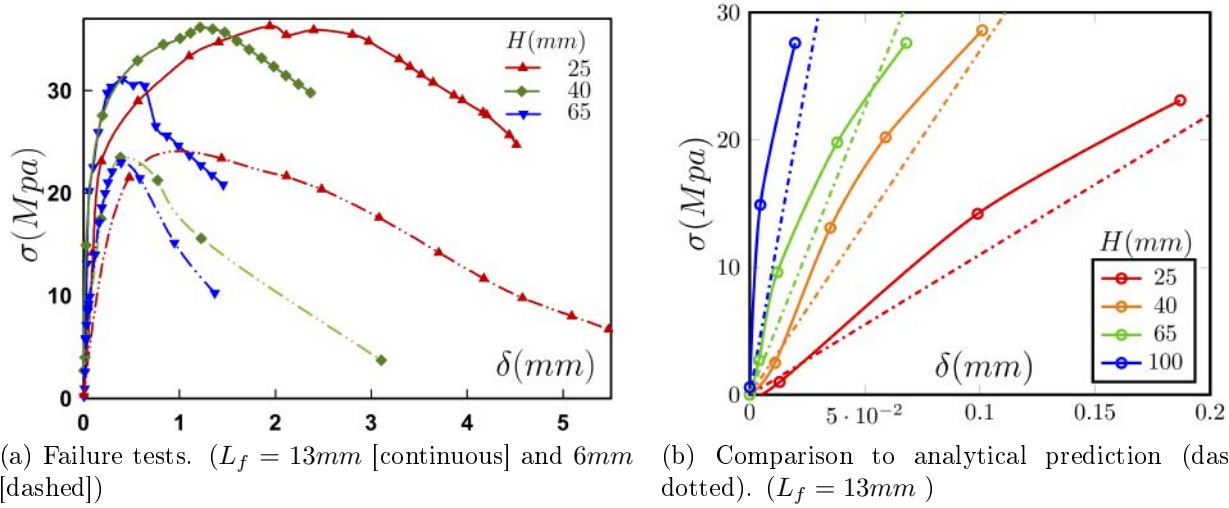


Figure 3: Stress-displacement diagrams.

During these intervals the load F and the corresponding displacements δ are recorded as well. Figure 3a represents the stress-displacement diagrams versus the geometry of the specimens and the fibre length, where the stress σ is simply computed with presumption of elastic behavior before initiation of cracks. (i.e. $\sigma = \frac{Mc}{I}$) Additionally Figure 3b shows the comparative study of the experimental curves before reaching the yield limit versus the analytical solution for stress displacement behavior.³The complete mathematical solution is provided in the Supplemental Information.

The steps in Figure 2 are detailed as follows:

1. The bare image has contains the information from the Red, Green and Blue values (i.e. $\{R, G, B\} \in [0, 255]$). I can turn to a normalized gray-scale intensity image by averaging the values as:

$$I_{i,j} = \frac{R_{i,j} + G_{i,j} + B_{i,j}}{3 \times 255}$$

where the $I_{i,j} \in [0, 1]$ is the intensity value of the obtained grayscale image.

2. The cracked regions (i.e. black) can be distinguished from solid concrete (i.e. white) by establishing a grayness threshold, $I_c \in [0, 1]$, which classifies matrix elements into black and white classes $\{B, W\} \in (0, 1)$. This value is determined iteratively from Otsu's method by minimizing the intra-class variance σ^2 as follows: [19]

³The error bars have been removed for the ease of observation.

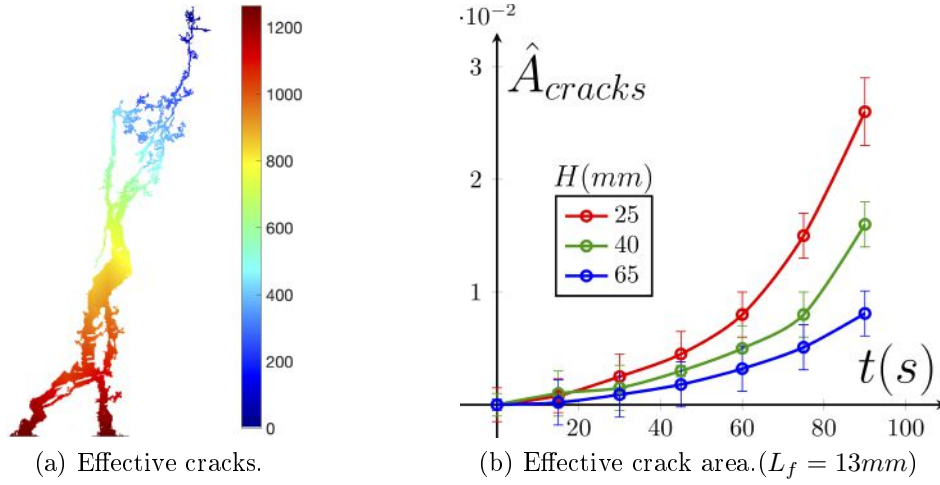


Figure 4: Percolation-based computation and tracing of effective cracks.

minimize σ^2 such that:

$$\begin{cases} \sigma^2 = \omega_1 \sigma_0^2 + \omega_2 \sigma_1^2 \\ \omega_1 + \omega_2 = 1 \end{cases} \quad (1)$$

where ω_1 and ω_2 are the fraction of black/white portions and σ_1^2 and σ_2^2 are the corresponding variances for each classified zone. Minimization of intra-class variance σ^2 ensures that the

obtained binarized image provides the best approximation of the original gray-scale image, as closest proximity for each chosen group is considered in the same class.

3. The augmented area (ΔA) in each stage ($\sim 15s$) could be obtained by percolating through the cracks from the bottom boundary until no further progress is made. [20] The incremental area difference ΔA^{k+1} can be obtained from the difference of two subsequent obtained images (i.e. Im^k, Im^{k+1}). Figure 1b represents the the captured effective cracks computed by the percolation from the surface. The values on the color-bar correlates with the distance from the instigation point of of the cracks. (i.e. surface).

Consequently we define the normalized computed crack area as a fraction of total (i.e. $\hat{A} := \frac{A_{cracks}}{A_{tot}}$) and track it versus time. Figure 4b represents such characterization, where the error-bars show the variation in 3 identical experimental setups.

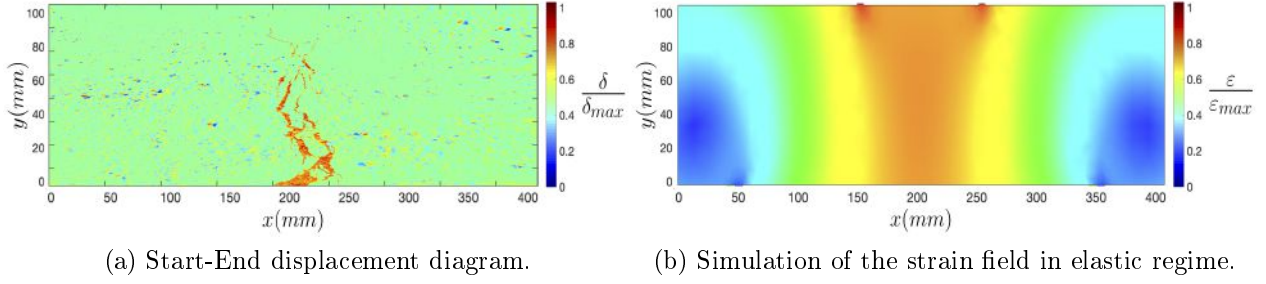


Figure 5: Correlation between the experiments/simulations.

4. The displacement field is additionally obtained from tracking the $\{R, G, B\}$ value of each element to it's closest proximity and extracting the corresponding displacement vector $V_{i,j}$ as well as its magnitude $I_{i,j}$.⁴ Figure 5a represents the *start-to-end* displacement field representing the evolved cracks as the most distinguishing compartments.

Additionally, we performed numerical simulation on the the four-point flexural load system via SolidWorks simulation package and have obtained the strain field on the linear regime for further analysis. the results are shown in the Figure 5b.

2.2 Analytical modeling

Figure 6 shows the schematics of an ideal, symmetric, and full fracture. The acting fibres are shown in red while others have turned inactive due to pull-out. The fibre efficacy measure (Λ) should in fact represent the role of *active* fibres involved in resisting the *effective* cracks. [21] During elastic mechanical behavior, the average fibre stress correlates with the localized strain value before the formation of cracks. However upon the fracture the strain field is relaxed and the elongation of fibers is mostly due to cracks. Therefore the efficacy measure Λ would depend on the crack opening. Due to geometry, during infinitesimal cracking, the opening of the crack w in flexural loading is correlated to the vertical distance y from the crack tip. For a general crack of random shape starting with the depth of y_0 the area would be:

$$A_{cracks} = \int_{y_0}^H w(y) dy \quad (2)$$

⁴ α is the scaling correction factor, relating the image value to the experimental magnitudes. In our study $\alpha = 2.5$.

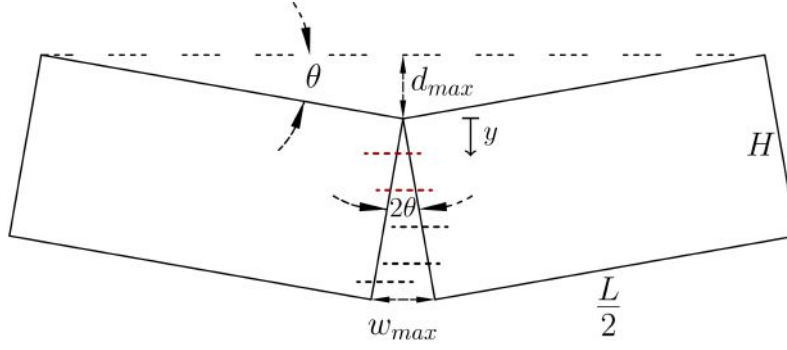


Figure 6: Schematics of ideal, symmetric, complete fracture.

126 Depending on if the fibres have reached this limit, they will either act elastic or plastic. The
 127 typical yield strain of the fibres is $\varepsilon_y \approx 0.001 - 0.002$ [22] mostly the plastic regime will occur:

128 i. Plastic zone:

129 In extended crack openings, the fibres are stretched till the post-yielding (plastic) stress
 130 ($\sigma(y) \approx \sigma_y$). For a crack ranging from the *tip-to-toe* in the span of y_0 to H , the absorbed
 131 energy for a fibre would be:

$$\delta E_{fib} = \sigma_y A_{fib} w$$

132 where A_{fib} is the cross sectional area of the fibre and can be expressed in terms of the fiber
 133 perimeter p_{fib} as $A_{fib} = p_{fib} \frac{d}{2}$ ⁵, and w is the local crack opening. Therefore the total
 134 absorbed energy in the fibres would be expressed as:

$$E_{fib} = \sum_{i=1}^n \sigma_y p_{fib} \frac{d}{2} w_i \quad (3)$$

135 As the fibres are highly packed, one can assume that they almost cover the entire surface
 136 area of the cracks. Therefore, since all the fibres have identical diameters and their heavy
 137 population covers the entire crack area, one can assume that $d := dy$ and we arrive at the
 138 following:

$$E_{fib} = \frac{1}{2} \int_{y_0}^H \sigma_y p_{fib} w(y) dy \quad (4)$$

⁵For circular cross section one has: $A_{fib} = \frac{\pi}{4} d^2 = \left(\frac{\pi d}{2}\right) \frac{d}{2} = p_{fib} \frac{d}{2}$.

139 Combining Equations 2 and 4 one has:

$$E_{fib,pl} = \frac{\sigma_y p_{fib}}{2} A_{cracks} \quad (5)$$

140 ii. Elastic zone:

141 Below yielding limit, for a crack opening with the tip at the depth of y_0 , we have a the
142 geometrical relationship due triangular inequality (Figure 6):

$$\frac{w(y)}{y - y_0} = \frac{w_{max}}{H - y_0} \approx \frac{2d_{max}}{L/2}$$

143 therefore the individual strain of each fibre is expressed as:

$$\epsilon(y) = \frac{w(y)}{L_f} = \frac{4d_{max}}{L_f L} (y - y_0)$$

144 and the energy absorbed in the individual fibre would be:

$$\delta E_{fib} = EA_{fib} \frac{16d_{max}^2}{L_f L^2} (y - y_0)^2$$

145 Thus the total absorbed energy in fibres would be integrated as:

$$E_{fib,el} = \left(\frac{20}{3} \frac{EA_{fib}}{L_f} \frac{H^3}{L^2} \right) \delta^2 \quad (6)$$

146 The original energy given to the beam by applying two externals loads F during the experi-
147 ment is:

$$E_{load} = 2F\delta \quad (7)$$

148 where δ is the corresponding displacement measured from the gages. Before the fracture,
149 the entire work (i.e. energy) from the loads is stored elastically within the beam. However
150 after the fracture all the beam is relaxed (unloaded) and the added energy is divided for the
151 formation of the crack E_{Crack} as well as the stretching of the fibres E_{fibers} as follows:

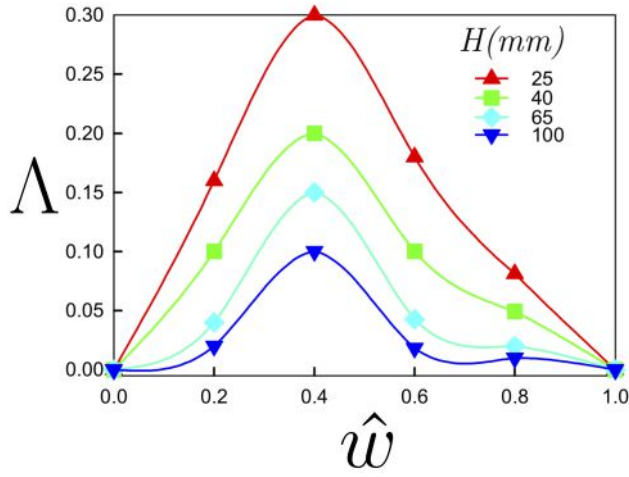


Figure 7: Evolution of Fibre efficacy Λ versus the normalized crack opening \hat{w} .

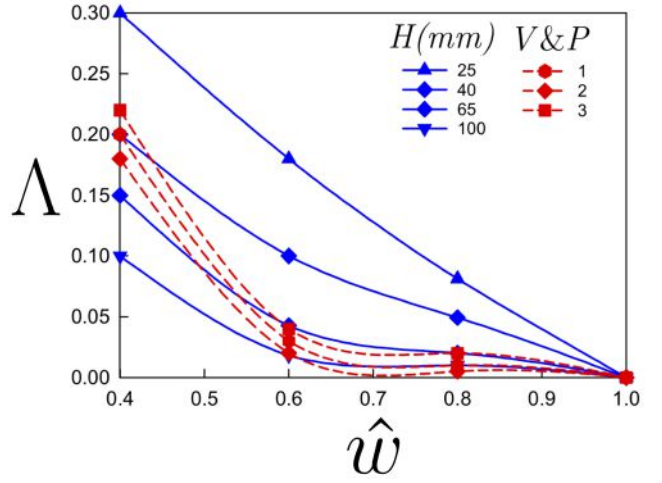


Figure 8: Late-stage correlation of the fibre efficacy Λ .

$$E_{total} = E_{crack} + E_{fibers} \quad (8)$$

which in fact proves that, the more the energy is transmitted to fibres, the less the crack surfaces form. Therefore the fibre efficacy factor Λ should describe what fraction of the absorbed energy within the plastic deformation of the fibres:

$$\Lambda = \frac{E_{fibres}}{E_{total}} \quad (9)$$

The evolution of fibre efficacy Λ versus the crack formation for our experimental prism beams is shown in Figure 7, assuming the plastic behavior of all the fibres (Equation 5) where the crack opening has been normalized to the fibre length as: $\hat{w} = \frac{w}{L_f}$. As well, the comparative study for the late-stage development of the cracks has been shown in Figure 8.

3 Results & Discussions

The stress-displacement diagram in Figure 3a reveals new information on role of the fiber length and geometry on the mechanical behavior. The reduction of the ultimate flexural strength versus the height of the beams reveals the deflection-softening behavior, whereas the initiation point of first cracks remain untouched as it represents the matrix performance.

On the contrary, the deflection hardening behavior has been observed in the thinner beams, representing size-effect role. [23] The energy absorption capacity (i.e. toughness) and deflection hardening capacity both decreased with beam height. The peaking of the load during the experiment, shows the toughening mechanism at the crack tip zone. The fibres become less effective with beam height, specially at peak of the load, where cracks become localized.

The comparison of the analytical and experimental trends in Figure 3b reveals that the experimental samples are show slightly higher strength (i.e. elastic modulus) than the analytical prediction for pure concrete. This is simply due to existence of the fibres embodied within the concrete, which in fact acts as a composite materials as a whole. In fact such a slight difference represents that the fibres are still active even before the initiation of the cracks.

While the heterogeneity of the FRC allows for the initiation of cracks possibly in multiple locations, the cracks starting from the boundary of the specimen are the most prone for causing the failure with a large margin relative to the others. Such a crack can be captured in our computation via percolating from the bottom of the specimen until no further progress is made (Figure 4a). The dynamics of propagation of the effective cracks in Figure 4b represents a runaway dynamics. Few reasons lie under such behavior, including the augmentation of the flexural stress. As the crack grows the resisting cross-section is decreases, which significantly reduces the second moment of inertia (i.e. $I \propto H^3$) and the flexural stress increases to a considerable extent. This causes rampant growth behavior in the cracks. For the same reason, the growth is more sensitive to the shorter specimen as has been obtained.

Analysis of the displacement diagram for the experimental cracked specimen in Figure 5a versus the computation of the strain map in elastic regime in Figure 5b reveals the consistency of the critical state in the middle bottom of the specimen, which is under tension. We note the highest localized strain values precisely under the loading points in Figure 5b would be neglected due to compression.

During pre-crack, the role of the fibres is in terms of the elastic shear transfer with matrix. However, upon the initiation of the cracks, their tensile behavior are activated and add up to the flexural resistance, leading to ductile behavior [24] and their effectiveness relies on the bridging within the formed crack. The frequency of such fibres increases with further

crack propagation and the fibre efficacy factor increases as shown in Figure 7. However upon extended crack openings, the fibres with shorter embedment lengths from one of the ends (at least) are successively pulled out and do not contribute any longer to the propagation resistance. Due to crack geometry, the frequency of such fibres decreases from the crack from the tip until the limit where the longest embedded fibre is pulled out. (Figure 6) The inception of the pull-out process in can be distinguished from locating the peaks of fibre efficacy Λ in the Figure 7, which occurs at $w \sim 0.4L_f$. This correlates highly with the reported value criterion of embedment length for effective bridging of $w_{max} < 0.5L_f$. [25, 26, 27], where the maximum number of the fibres are effectively bridging the crack. Nonetheless, the slight less value of in our development shows that a small fraction of the fibres could in fact pull out before reaching the typical limit.

The late-stage behavior of the fibre efficacy measure Λ versus the normalized crack opening \hat{w} , (Figure 8) which occurs after pull-out process, correlates highly with the reported values. [28] Both values correlate and gradually reduce with crack progress as shown in Figure 8. Additionally, both values approach zero when crack width tends to Fibre length ($w \approx L_f$). Nevertheless, our slightly higher values in Figure 8 would be due our assumption of yielding the bridging fibres, which is more effective than frictional (i.e. pull-out) mechanism. Such decreasing trend versus crack progress has also previously reported as well. [29, 30, 31] Additionally, it was observed that thinner beams posses improved bridging, which is plausible since they have more uniform fibre density and homogeneity in fibre-orientation than the thicker beams during fabrication and their work of fracture is considerably reduced. [32] Needless to mention that the variation in the curvature in our results and the literature has interesting correlations as well, which is more apparent with the comparison of the literature trend in Figure 8 with the post-peak behavior in Figure 7.

4 Conclusions

In this paper, we have introduced a new measure Λ for quantification of the effectiveness for fibres in the FRC during the full course of crack instigation and propagation. We performed percolation-based modeling for computing the effective area of the cracks and we established

a model based on the absorbed energy of the fibres. Upon the instigation of the infinitesimal cracks and activation of the fibres, the fibre efficacy has increased and reached to the peak value. After the pull out process, the efficacy value has been reduced, concurrent in the literature. The better performance of the lower-scale beams represents more proper spatial distribution of fibres, leading to effective bridging. Our developed measure can be used to quantify fibres performance in FRC beams versus cracks area for any propagation patterns.

References

- [1] Marco Di Prisco, Giovanni Plizzari, and Lucie Vandewalle. Fibre reinforced concrete: new design perspectives. *Mater. Struct.*, 42(9):1261–1281, 2009.
- [2] Joost C Walraven. High performance fiber reinforced concrete: progress in knowledge and design codes. *Mater. Struct.*, 42(9):1247, 2009.
- [3] Mirosław Grzybowski and Surendra P Shah. Shrinkage cracking of fiber reinforced concrete. *Materials Journal*, 87(2):138–148, 1990.
- [4] N Banthia, M Azzabi, and M Pigeon. Restrained shrinkage cracking in fibre-reinforced cementitious composites. *Mater. Struct.*, 26(7):405–413, 1993.
- [5] KCG Ong and P Paramasivam. Cracking of steel fibre reinforced mortar due to restrained shrinkage. *Fibre Reinforced Cements and Concretes: Recent Developments*, pages 179–187, 1989.
- [6] Arnon Bentur and Sidney Mindess. *Fibre reinforced cementitious composites*. CRC Press, 2014.
- [7] Ingemar Löfgren. *Fibre-reinforced Concrete for Industrial Construction-a fracture mechanics approach to material testing and structural analysis*. Chalmers University of Technology, 2005.
- [8] James P Romualdi and James A Mandel. Tensile strength of concrete affected by uniformly distributed and closely spaced short lengths of wire reinforcement. In *Journal Proceedings*, volume 61, pages 657–672, 1964.

- [9] Syed Yasir Alam, Jacqueline Saliba, and Ahmed Loukili. Fracture examination in concrete through combined digital image correlation and acoustic emission techniques. *Constr. Build. Mater.*, 69:232–242, 2014.
- [10] SG Shah and JM Chandra Kishen. Fracture properties of concrete-concrete interfaces using digital image correlation. *Exp. Mech.*, 51(3):303–313, 2011.
- [11] İrem Şanal, Nilüfer Özyurt Zihnioğlu, and Ardalan Hosseini. Particle image velocimetry (piv) to evaluate fresh and hardened state properties of self compacting fiber-reinforced cementitious composites (sc-frccs). *Constr. Build. Mater.*, 78:450–463, 2015.
- [12] Ardalan Hosseini, Davood Mostofinejad, and Masoud Hajjalilue-Bonab. Displacement and strain field measurement in steel and rc beams using particle image velocimetry. *J. Eng. Mech.*, 140(11):04014086, 2014.
- [13] Anette Jansson, Mathias Flansbjer, Ingemar Löfgren, Karin Lundgren, and Kent Gylltoft. Experimental investigation of surface crack initiation, propagation and tension stiffening in self-compacting steel–fibre-reinforced concrete. *Mater. Struct.*, 45(8):1127–1143, 2012.
- [14] RC Bradt. Problems and possibilities with cracks in ceramics. In *Proc. 11 th International Conf. on Science of Ceramics held at Stenungsund, Sweden, June 14-17, 1981. Edited by R. Carlsson and S. Karlsson. Swedish Ceram. Soc., Gothenburg, Sweden, 1981.*, page 349, 1981.
- [15] Wang Zhan-Qiao. *Testing research on the fracture properties of fiber reinforced high-strength concrete*. PhD thesis, MS thesis, Zhengzhou University, 2004.
- [16] MÁRIO PIMENTEL, AMIN ABRISHAMBAF, and SANDRA NUNES. Anisotropic tensile behaviour of uhpfrc: Meso-scale model and experimental validation.
- [17] Tong-qing LU and Jia-jie LONG. The application of synthetic fibers in concrete [j]. *Journal of Suzhou Institute of Silk Textile Technology*, 2:010, 2005.
- [18] Guo Yong-chang and Zhang Hong-Zhou. Research and engineering applications of fiber-reinforced concrete. *Guangdong Building Materials*, 7:8–9, 2004.

- [19] Nobuyuki Otsu. A threshold selection method from gray-level histograms. *Automatica*, 11(285-296):23–27, 1975.
- [20] Asghar Aryanfar, William Goddard III, and Jaime Marian. Constriction percolation model for coupled diffusion-reaction corrosion of zirconium in pwr. *Corrosion Science*, 2019.
- [21] Herbert Krenchel. *Fibre spacing and specific fibre surface*. 1975.
- [22] BK Behera and PK Hari. 7-tensile behavior of woven fabrics. *Woven Textile Structure*, pages 137–163, 2010.
- [23] Duy Liem Nguyen, Dong Joo Kim, Gum Sung Ryu, and Kyung Taek Koh. Size effect on flexural behavior of ultra-high-performance hybrid fiber-reinforced concrete. *Composites Part B: Engineering*, 45(1):1104–1116, 2013.
- [24] Thomas Pfyl. *Tragverhalten von stahlfaserbeton*, volume 279. vdf Hochschulverlag AG, 2003.
- [25] Ekkehard Fehling, Michael Schmidt, Joost Walraven, Torsten Leutbecher, and Susanne Fröhlich. *Ultra-high performance concrete UHPC: Fundamentals, design, examples*. John Wiley & Sons, 2014.
- [26] P Rossi and G Chanvillard. 5th rilem symposium on fibre reinforced concretes (befib 2000). *Cachan, France: RILEM Publications*, 2000.
- [27] Filipe Laranjeira de Oliveira. *Design-oriented constitutive model for steel fiber reinforced concrete*. Universitat Politècnica de Catalunya, 2010.
- [28] Emmanouil Vougioukas and Maria Papadatou. A model for the prediction of the tensile strength of fiber-reinforced concrete members, before and after cracking. *Fibers*, 5(3):27, 2017.
- [29] Christian O Sorensen, Egil A Berge, Petter E Saga, and Andreas Østvold. Factors affecting the efficiency of fibers in concrete on crack reduction. *Open Journal of Civil Engineering*, 3(02):80, 2013.

[30] Nicola Buratti, Claudio Mazzotti, and Marco Savoia. Post-cracking behaviour of steel and macro-synthetic fibre-reinforced concretes. *Constr. Build. Mater.*, 25(5):2713–2722, 2011.

[31] Peter Baltay and Atle Gjelsvik. Coefficient of friction for steel on concrete at high normal stress. *J. Mater. Civ. Eng.*, 2(1):46–49, 1990.

[32] Yougui Lin and John N Karadelis. Establishing the fiber bridging law by an inverse analysis approach. *J. Mater. Civ. Eng.*, 28(2):04015105, 2015.

Supplemental Information

The basic development for the deflection of the beam is as follows:

$$\frac{\partial^2 y}{\partial x^2} = \frac{M}{EI}$$

For simplicity in integration, one can define the Heaviside function as below:

$$< x - a > = \begin{cases} x - a & x \geq a \\ 0 & x < a \end{cases}$$

the reactions are no-deflection points, therefore $y(a) = y(7a) = 0$. From Figure 1a the moment is obtained as:

$$M = F < x - a > - F < x - 3a > - F < x - 5a > + F < x - 7a >$$

Consequently, the deflection could be obtained by double integrating as:

$$y = \frac{F}{6EI} (< x - a >^3 - < x - 3a >^3 - < x - 5a >^3 + < x - 7a >^3) + c_1 x + c_2$$

Replacing the boundary condition into the above equation:

$$\begin{cases} c_1 a + c_2 = 0 \\ \frac{F}{6EI} (216a^3 - 64a^3 - 8a^3) + 7c_1 a + c_2 = 0 \end{cases} \Rightarrow \begin{cases} c_1 = -\frac{4Fa^2}{EI} \\ c_2 = \frac{4Fa^3}{EI} \end{cases}$$

315 and the deflection curve is obtained as:

$$y = \frac{F}{6EI} (< x - a >^3 - < x - 3a >^3 - < x - 5a >^3 + < x - 7a >^3 - 24a^2(x - a))$$

316 where the deflection values under the loads would be:

$$\delta_1 = \delta_2 = -\frac{20}{3} \frac{Fa^3}{EI} = -\frac{10Ma^2}{EI} = -\frac{5a^2}{EH} \sigma$$

317 This equation represents the analytical relationship for the stress σ and the displace-
 318 ment δ , versus the geometrical parameter H , which is used in Figure 3b⁶. Additionally the
 319 maximum displacement occurs in the center as:

$$\delta_{max} = y(4a) = -\frac{23}{3} \frac{Fa^3}{EI}$$

⁶In fact the absolute value is of the interest.